Journal of Instrumentation

J-PARC 3-GeV RCS: 1-MW beam operation and beyond

Published by IOP Publishing for Sissa Medialab

Received: *May 29, 2020*
Accepted: *June 2, 2020*
Published: *July 22, 2020*

ICFA Beam Dynamics Newsletter#79 — Space Charge

2020 JINST 15 P07022

J-PARC 3-GeV RCS: 1-MW beam operation and beyond

H. Hotchi,[1] H. Harada, N. Hayashi, M. Kinsho, K. Okabe, P.K. Saha, Y. Shobuda, F. Tamura, K. Yamamoto, M. Yamamoto and M. Yoshimoto

Accelerator Division, J-PARC Center, Japan Atomic Energy Agency (JAEA), Tokai, Naka, Ibaraki 319-1195 Japan

E-mail: hideaki.hotchi@j-parc.jp

Abstract: The J-PARC 3-GeV rapid cycling synchrotron (RCS) has recently achieved a 1-MW beam operation with considerably low fractional beam loss of a couple of 10^{-3} as a result of continuous efforts iterating experiments and numerical simulations. This success of the 1-MW beam operation opened a door to further beam power ramp-up beyond 1 MW; we are now promoting $1.2 \sim 1.5$-MW-equivalent high-intensity beam tests looking ahead to future upgrades at J-PARC. In this article, we first review the current status of beam loss in the 1-MW beam operation, then presenting the recent results of the 1.2-MW beam tests with particular emphasis on our approaches to beam loss issues. The beam intensity limit of the RCS is also discussed with well-established numerical simulations.

Keywords: Accelerator modelling and simulations (multi-particle dynamics; single-particle dynamics); Beam dynamics

[1]Corresponding author.

https://doi.org/10.1088/1748-0221/15/07/P07022

Contents

1 Introduction

The J-PARC 3-GeV Rapid Cycling Synchrotron (RCS) is a world leading high-power pulsed proton driver, which has the goal of achieving a 1-MW beam power (8.33×10^{13} protons per pulse at 25 Hz) [1–3]. Figure 1 shows the layout of the RCS. As shown in the figure, a 400-MeV negative hydrogen ion (H^-) beam from the injector linac is delivered to the RCS injection point, where it is multi-turn charge-exchange injected through a carbon foil over a period of 0.5 ms (307 turns). The RCS accelerates the injected protons up to 3 GeV with a repetition rate of 25 Hz, providing the high-power beams both to the Materials and Life Science Experimental Facility (MLF) and the Main Ring (MR) while switching the beam destination pulse by pulse.

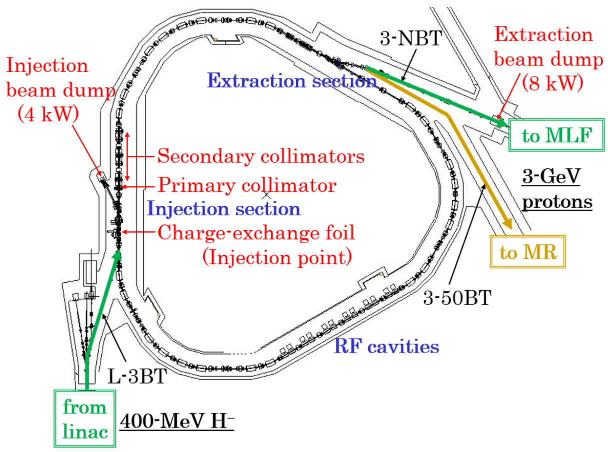

Figure 1. Layout of the J-PARC 3-GeV RCS.

The most important issues in realizing such a MW-class high-power beam operation are controlling and minimizing beam loss to maintain machine activations within permissible levels. In high-power machines such as the RCS, space charge and its combined effects with lattice imperfections are mentioned as a major source of beam loss. In the RCS, numerical simulation [4] was successfully utilized along with experimental approaches to isolate such beam loss mechanisms and find their solutions. By iteratively performing actual beam experiments and numerical simulations, we have successfully reduced beam loss in the 1-MW beam operation to a couple of 10^{-3} [3]. The routine RCS beam power for users is still limited to 500 kW due to a delay in the development of the neutron production target capable of withstanding MW-class high-power beams, but the accelerator itself is ready for the routine 1-MW beam operation.

Following the success of the 1-MW beam tuning, we have recently initiated further high-intensity beam tests aiming for a higher beam power beyond 1 MW, looking ahead to future upgrades at J-PARC. The initial goal is to achieve 1.2 $\sim$ 1.5-MW-equivalent (eq) high-intensity beam accelerations within permissible beam loss levels, increasing the injection pulse length from 0.5 ms to 0.6 ms, and/or increasing the injection peak current from 50 mA to > 60 mA.

In this article, we first review the current status of beam loss in the 1-MW beam operation, and then, present our recent efforts towards a higher beam power beyond 1 MW with particular emphasis on our approaches to beam loss issues. Finally, we discuss the intensity limit of the RCS, based on numerical simulations.

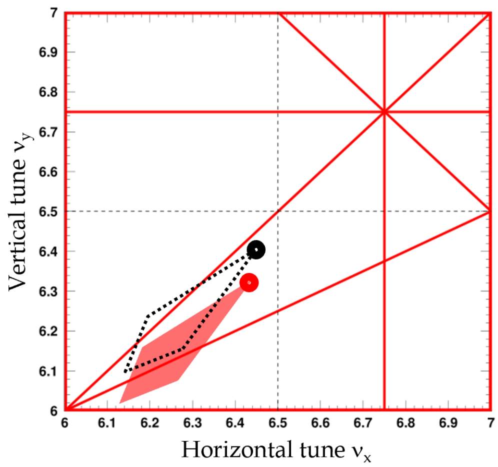

Figure 2. Tune diagram near the operating point, where the red lines show the structure resonances up to the 4th order, derived from the three-fold symmetric lattice of the RCS.

2 Current status of beam loss in the 1-MW beam operation

We started a 1-MW beam test in Oct. 2014 just after completing the injector linac upgrades, and achieved the 3-GeV acceleration in Jan. 2015 via the success of beam loading compensation for such a high-intensity beam [5]. Since then, we have continued the beam studies for beam loss mitigation. In this section, we first briefly review the 1-MW beam tuning for beam loss mitigation, and then, discuss the mechanism of the beam loss presently left.

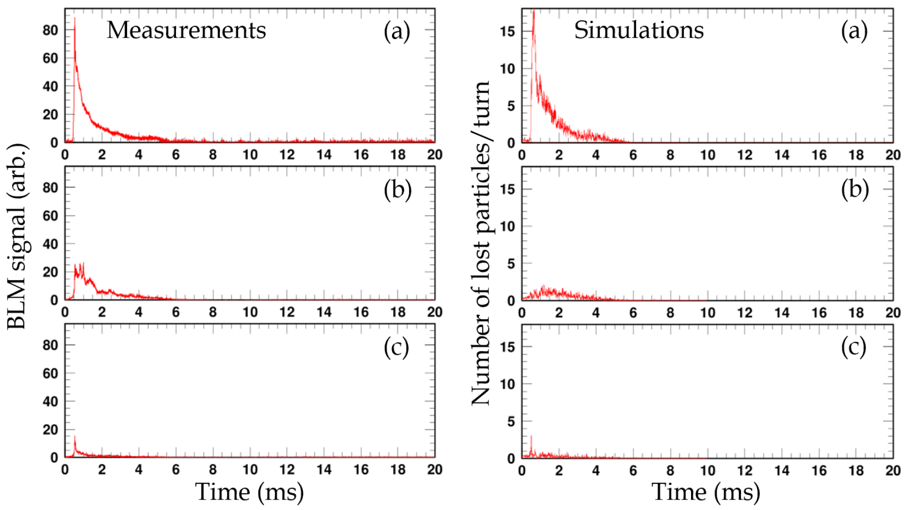

Figure 3. (Left) Beam loss monitor signals measured at the collimator section. (Right) Corresponding numerical simulation results.

2.1 Efforts for beam loss mitigation

Figure 2 shows the tune diagram. We started 1-MW beam tuning in the vicinity of the black circle in the figure; $(6.45, 6.38) \sim (6.45, 6.42)$. For this operational condition, $\sim$ 2%-significant beam loss occurred, as shown in the left panel (a) of figure 3. This operating point allows tune shifts to avoid serious structure resonances, such as low-order one-dimensional resonances and coupling-sum resonances, which are directly connected with beam loss. In exchange for this, however, the operating point is very close to the Montague resonance $2\nu_x - 2\nu_y = 0$. This resonance is well known to cause space-charge-induced emittance exchange [6, 7]. As shown in the right panel (a) of figure 3, the numerical simulation well reproduced the experimental beam loss, and revealed that the $\sim$2% beam loss is caused by the emittance exchange [8]. The left panel (a) in figure 4 represents a 2-dimensional space of the horizontal and vertical actions (J_x, J_y), showing the mechanism of the beam loss. In this figure, the yellow arrow shows the path of injection painting applied for space-charge mitigation [9]; the injection beam is filled from the middle to the outside on both the horizontal and vertical planes over the painting area of 200π mm mrad. To this direction of injection painting, the emittance exchange ($J_x - J_y$ exchange of a single particle) occurs in the orthogonal direction, as shown by the red arrow, namely, in a direction parallel with the line of J_x+J_y=const. The right panel (b) in figure 4 shows scatter plots of (J_x, J_y) at the end of injection painting, calculated without and with space charge. Comparing them, one can find that the space charge makes a significant diffusion of beam particles away from the path of injection painting, leading to a critical increase of the peak J_y of beam particles. In addition, in figure 5, one can confirm that it is caused by the emittance exchange that occurs perpendicularly to the path of injection painting. The growth of the maximum J_y of the beam particles caused by the emittance exchange is the main cause of the beam loss observed in the left panel (a) of figure 3. Though the mechanism of the Montague resonance can be considered as a combination of incoherent and coherent resonance phenomena, the coherent effect is less important in this case, because the injection painting applied in the present work approximately maintains the isotropic condition (equal rms emittances on the

2020 JINST 15 P07022

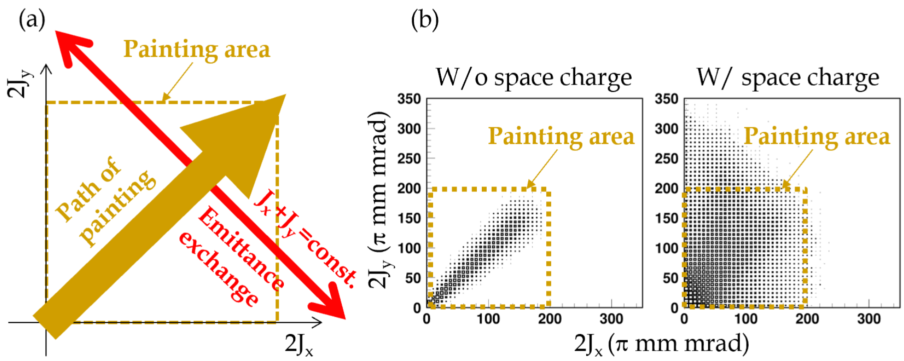

Figure 4. (a) Schematic illustration of the geometrical relationship between injection painting and emittance exchange in the (J_x, J_y) space. (b) Numerical simulation results; scatter plots of (J_x, J_y) at the end of injection painting calculated without (left) and with (right) space charge.

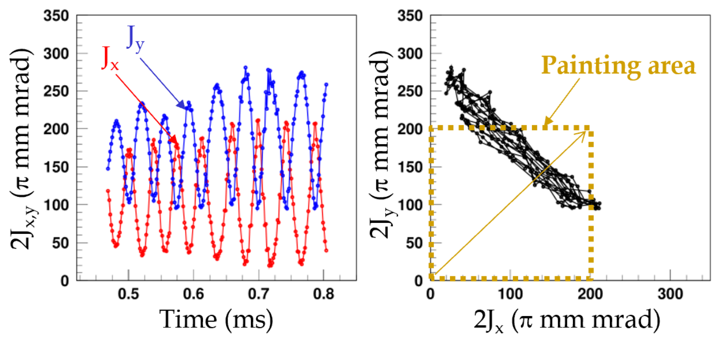

Figure 5. Numerical simulation results; single-particle motion of one macro-particle; J_x and J_y as a function of time (left), and their trajectory in the (J_x, J_y) space (right).

horizontal and vertical planes) throughout. Consequently, the behavior of the beam particles in figures 4 and 5 can mainly be ascribed to the incoherent effect of the Montague resonance that is driven by the existing space-charge coupling term.

In order to improve the above situation, the operating point was changed to (6.43, 6.32), as shown in figure 2, which is sufficiently far from the Montague resonance. This operating point mitigated the detrimental effect of the Montague resonance, significantly reducing the beam loss from (a) to (b) in the left panel of figure 3. But, instead, the modified operating point enhanced the effect of the 3$^{\text{rd}}$-order resonance $\nu_x - 2\nu_y = -6$ on the beam, as shown in figure 2. The 3$^{\text{rd}}$-order resonance is mainly driven by the sextupole field components inherent in the main bending magnets ($K_2 = -0.10\,\text{m}^{-2}$), causing emittance exchange similarly to the case of the Montague resonance but in a direction parallel with the line of $2J_x + J_y = \text{const}$ in the (J_x, J_y) space; $J_x - J_y$ exchange with a ratio of $\Delta J_y/\Delta J_x = -2$. Accordingly, it has the effect of increasing the peak J_y of beam particles. This is the main cause of the residual beam loss observed in the left panel (b) of figure 3. The driving term of the 3$^{\text{rd}}$-order resonance is now well compensated with two families of sextupole magnets, by which the beam loss was significantly reduced from (b) to (c) in the left panel of figure 3. By this series of beam tuning, the beam loss in the 1-MW beam operation was successfully reduced to a few times 0.1% only around the injection energy.

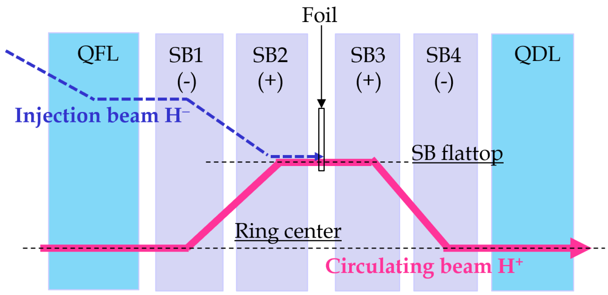

Figure 6. Schematic illustration of the injection section.

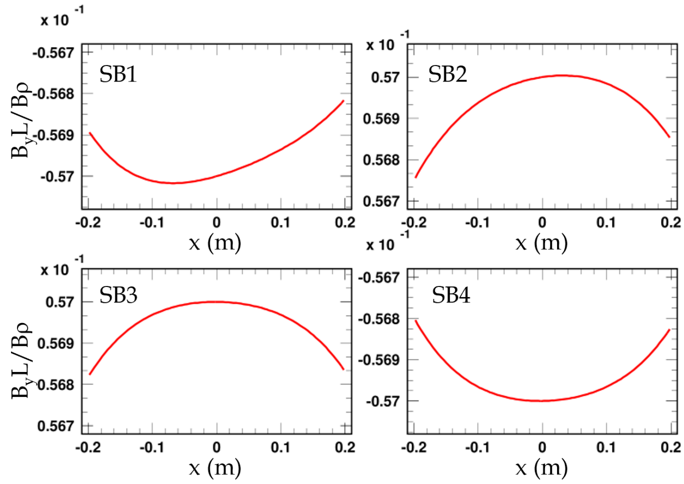

Figure 7. Magnetic field distributions measured for the SB 1, 2, 3, and 4.

2.2 Mechanism of the residual beam loss

As shown in the right panel of figure 3, the numerical simulations well reproduced the experimental beam losses, and found out two major sources of the residual beam loss (c) of a couple of 10^{-3}.

One is the effect of the $3\nu_x = 19$ resonance driven by the sextupole field components intrinsic in the injection bump magnets [10]. As shown in figure 6, four sets of same-type pulsed dipole magnets, SB1-4, are utilized for forming a horizontal injection orbit bump of Δx=101 mm; they are excited over 0.5 ms (307 turns) for multi-turn injection, and then sharply turned down within the following 0.35 ms. Figure 7 shows the magnetic field distributions measured for the SB 1, 2, 3, and 4 [11–13], in which one can clearly see that each SB has a significant sextupole field component. Ideally, the SBs generate the same magnetic field distribution except polarity. That is, the SB fields, including the high-order field components, cancel out each other through integration over the four injection bump magnets. In such an ideal case, the SB fields have no significant influence on the beam, but in practice, it is different. As shown in figure 6, the SBs are installed very close to one another. Besides, the distances of SB2-3 and SB1-2 (SB3-4) are different. In addition, the SB1 and SB4 are also very close to the quadrupole magnets (QFL and QDL). Due to such situations in reality, each SB has different magnetic interferences with its neighboring components. Therefore, the actual field distributions of the SBs are not identical. In the actual beam operation, the SB fields are adjusted so that the local orbit bump is closed precisely, namely so that the dipole field component, which the beam feels through the SB1-4, is compensated completely. But, as to the higher-order field components, such a field compensation is incomplete due to the effects of the magnetic interferences. The residual sextupole field component ($K_2 = 0.006\,\mathrm{m}^{-2}$), not canceled out, excites the $3\nu_x = 19$ resonance, affecting the circulating beam during multi-turn injection.

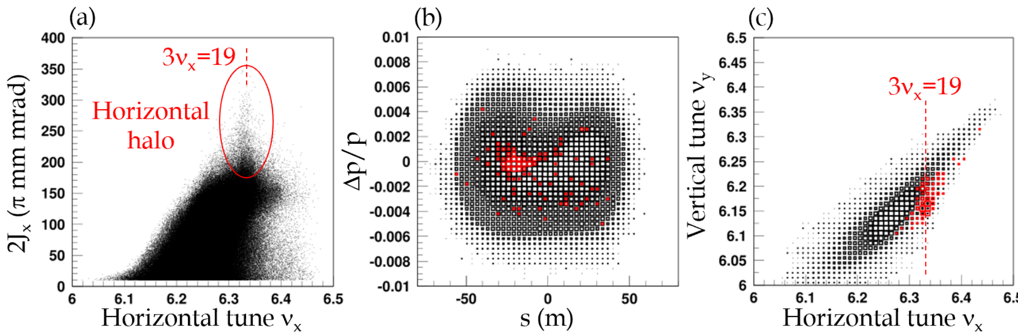

Figure 8. Numerical simulation results; (a) scatter plot of the horizontal tune and horizontal action, (b) longitudinal phase space, and (c) tune footprint, calculated at the end of injection, where the particles painted red in (b) and (c) correspond to the beam halo particles found in (a).

Figure 8 (a) shows a scatter plot of the horizontal tune and horizontal action calculated at the end of injection, in which one can find that a beam halo is generated horizontally on the $3\nu_x = 19$ resonance. In order to comprehend which particles suffer the effect of the $3\nu_x = 19$ resonance most intensely, we looked into the correlation between the beam halo formation and the longitudinal motion of the beam. Figures 8 (b) and (c) show the longitudinal phase space and the tune footprint calculated at the end of injection, where the particles painted red correspond to the beam halo particles found in (a). As shown in the figure, most of the beam halo particles move around the middle of the longitudinal phase space. The momentum deviations $\Delta p/p$ of such particles do not change widely during synchrotron motion, so the turn-by-turn change of their chromatic tune shift is restrictive. In addition, the effects of space charge on such particles are almost constant during synchrotron motion owing to a flat bunch distribution which is formed by longitudinal injection painting [14, 15]. Accordingly, the turn-by-turn change of their space-charge tune shift is also restrictive. That is, the tunes of particles in the middle region of the longitudinal phase space do not change widely turn by turn. As shown in figure 8 (c), a part of such inactive particles stays near the $3\nu_x = 19$ resonance for a relatively long time, and continuously or frequently suffers the effect of the resonance. This is the mechanism of the horizontal beam halo formation observed in figure 8 (a), and it makes a part of the residual beam loss.

Another source of the remaining beam loss is the residual effect of the $\nu_x - 2\nu_y = -6$ resonance on off-momentum particles. In figure 9, (a) shows a scatter plot of the vertical tune and vertical action, while (b) shows the longitudinal phase space, where the particles painted red correspond to the large amplitude particles found on the vertical plane in (a). As shown in the figure, most of the large amplitude particles move around the outer region of the longitudinal phase space. That is, they are off-momentum particles. We investigated the detailed behavior of such particles, and found that the effect of $\nu_x - 2\nu_y = -6$ on off-momentum particles generates the vertical beam

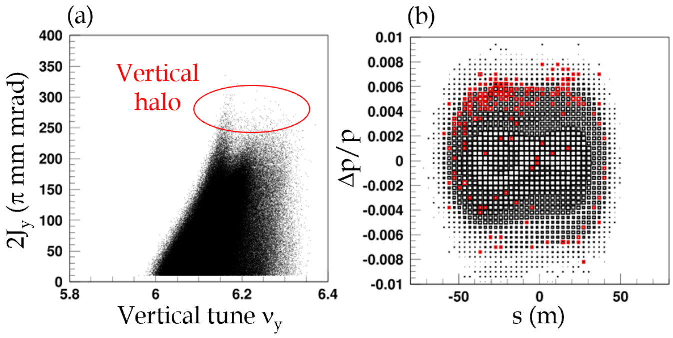

Figure 9. Numerical simulation results; (a) scatter plot of the vertical tune and vertical action, and (b) longitudinal phase space, calculated at 1.2 ms, where the particles painted red in (b) correspond to the beam halo particles found in (a).

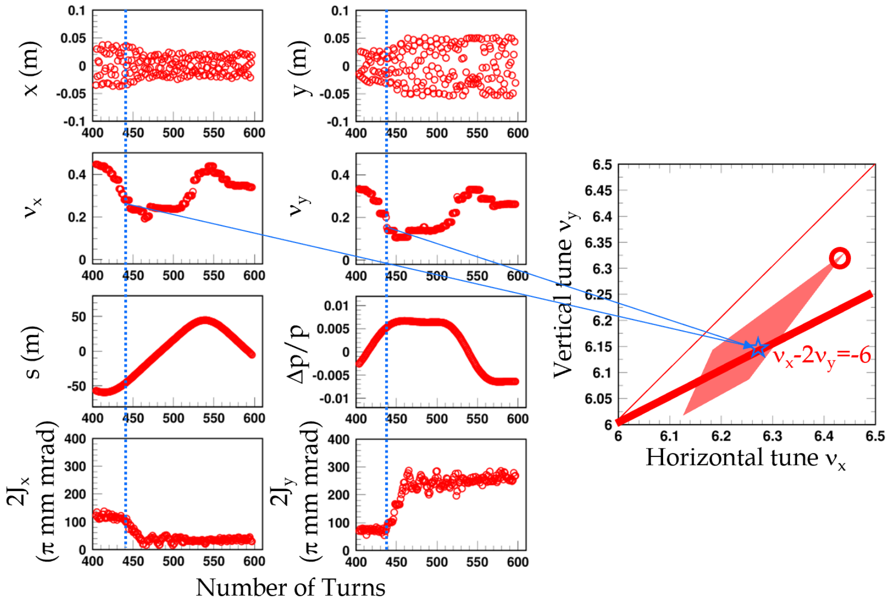

Figure 10. Numerical simulation results; turn-by-turn single-particle motion of an off-momentum particle leading to the vertical beam halo in figure 9 (a).

halo. Figure 10 shows the turn-by-turn single-particle motion of an off-momentum particle leading to the vertical beam halo. As shown in the figure, the tune of the particle changes as per the synchrotron oscillation. In this process, one can find that emittance exchange ($J_x - J_y$ exchange with a ratio of $\Delta J_y/\Delta J_x = -2$) occurs at the timing (blue dotted lines) when the tune gets on the $\nu_x - 2\nu_y = -6$ resonance. As already mentioned, the resonance correction is already applied for the 3$^{\text{rd}}$-order resonance with two families of sextupole magnets. But it is just for on-momentum particles; the effect of the resonance is still left for off-momentum particles. Such a residual effect of the resonance causes the vertical beam halo found in figure 9 (a). This is another mechanism of the residual beam loss.

As mentioned above, there still remains a certain amount of beam loss, but it is now acceptably small; a couple of 0.1% in the injection energy region. Most of the residual beam loss is well localized at the collimator section; besides the beam loss power is less than 1/10 the capability of the collimator system (4 kW). Therefore, we do not expect the residual beam loss to lead to serious issues. In fact, we had no notable increases in the machine activations after a continuous 10-hour 1-MW beam demonstration at 25 Hz. It can be said that the accelerator itself including the linac is ready for the routine 1-MW user operation.

3 1.2-MW-eq high-intensity beam tests

The success of the 1-MW beam tuning opened a door to a further beam power ramp-up. Looking ahead to future upgrades at J-PARC, we have recently initiated further high-intensity beam tests aiming for a higher beam power beyond 1 MW. First, we conducted a beam test increasing the injection pulse length from 0.5 ms to 0.6 ms in Oct. 2018, and then, we performed a similar beam test increasing the injection peak current from 50 mA to 60 mA in Dec. 2018. The beam intensity reached 1.0×10^{14} protons per pulse in both cases, which correspond to a 1.2-MW beam power if running at 25 Hz. In this section, we present these experimental results, especially focusing on our efforts for beam loss mitigation.

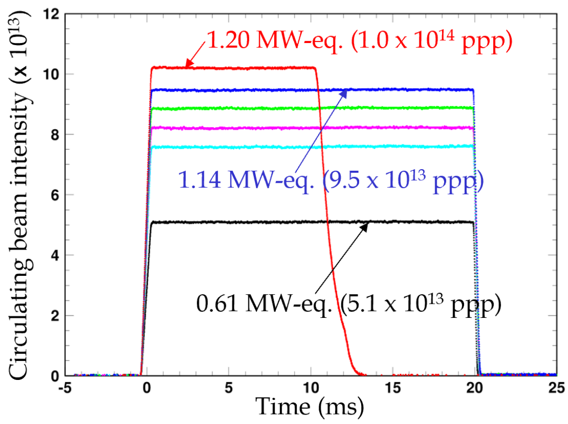

Figure 11. Circulating beam intensities from injection to extraction.

3.1 Initial acceleration test

Figure 11 displays the result of the high-intensity beam test with the longer injection pulse of 0.6 ms, showing the circulating beam intensity from injection to extraction. In this beam test, we gradually increased the beam intensity from 0.6 MW to 1.2-MW-eq. As shown in the figure, we achieved a 3-GeV acceleration for the beam intensities of up to 1.1-MW-eq, but not for the 1.2-MW beam, as illustrated by the red curve. This was due to an rf trip by the interlock. For higher beam intensity, larger beam loading compensation is needed. The required rf power for the 1.2-MW beam acceleration exceeded its power supply limit. To realize a 3-GeV acceleration for this beam intensity or more, we need several hardware upgrades for the rf system [16, 17].

In this beam test, however, we achieved a beam acceleration of up to ~1.5 GeV for the 1.2-MW beam. Beam loss usually occurs in the low energy region below 1 GeV, so we were able to conduct a sufficient beam loss study even for the 1.2-MW beam. At the start of the beam study for the 1.2-MW

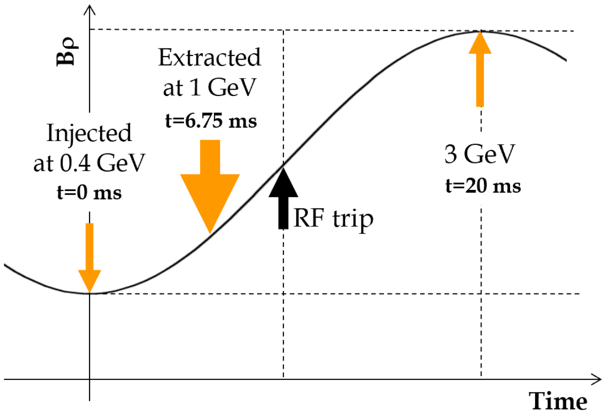

Figure 12. Schematic illustration of the 1-GeV extraction.

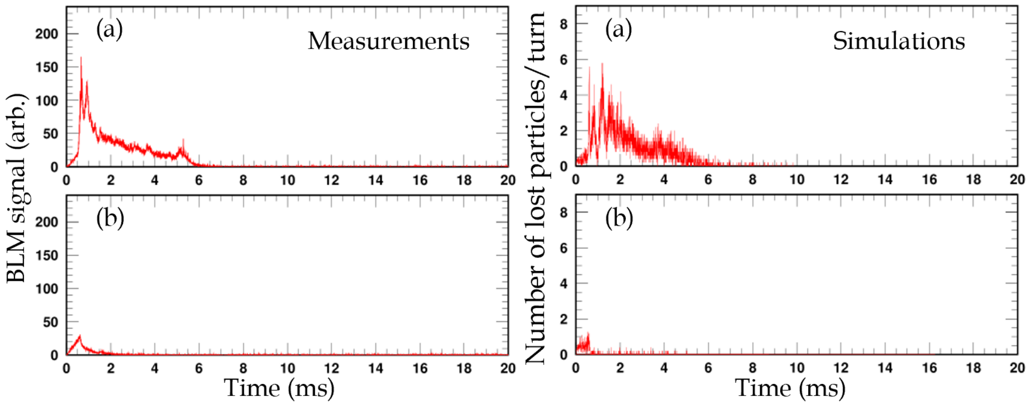

Figure 13. (Left) Beam loss monitor signals measured at the collimator section. (Right) Corresponding numerical simulation results.

beam, we established a 1-GeV extraction to avoid unnecessary rf trips, as shown in figure 12; the beam was extracted at 1 GeV before the rf trip, and properly transported to the extraction beam dump. After establishing this system, we performed a detailed beam loss study for the 1.2 MW beam. As is shown later, the beam loss appeared only for the first 6 ms, namely, within the region below 1 GeV. Thus, we could carry out a sufficient beam loss study even under this experimental condition.

3.2 Parameter optimizations for beam loss mitigation

First, we confirmed the beam loss for the 1.2-MW beam, applying the operational parameters optimized for the 1-MW beam as it is. As shown in the left panel (a) of figure 13, ~1%-significant beam loss occurred for this operational condition. The numerical simulation closely reproduced the experimental beam loss as shown in the right panel (a) of figure 13. Using the numerical simulation result, we discussed the beam loss mechanism and its solution.

As illustrated by the black circle in figure 14, the operating point was first set at (6.43, 6.32). In this case, a core part of the 1.2-MW beam crosses the integer $\nu_y = 6$. On this integer, all-order systematic resonances are excited. That is, strong stopbands exist around the integer. The numerical

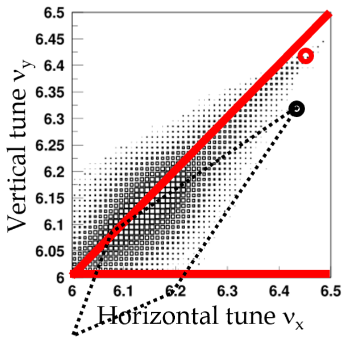

Figure 14. Numerical simulation result; tune footprint calculated at the end of injection.

simulation suggested that the beam loss observed in the left panel (a) of figure 13 mainly comes from a vertical emittance growth caused by the stopbands (the effect of the stopbands will be discussed in more detail in the next section). In order to improve the situation, the operating point was changed to $(6.45, 6.42)$, as illustrated by the red circle in figure 14. The modified operating point has a larger separation from the integer, but in exchange for this, it is very close to the Montague resonance $2\nu_x - 2\nu_y = 0$. As already discussed in figures 4 and 5, the emittance exchange driven by the Montague resonance diffuses beam particles away from the path of injection painting in the (J_x, J_y) space, causing beam loss. As is evident from figure 4 (a), the scale of the diffusion of beam particles in the (J_x, J_y) space is proportional to the painting area. Therefore, to mitigate such an effect of the Montague resonance, the painting area was slightly reduced from 200π to 150π mm mrad. By these treatments for $\nu_y = 6$ and $2\nu_x - 2\nu_y = 0$, the beam loss was successfully reduced to the order of 10^{-3} even for the 1.2-MW beam, as predicted by the numerical simulation displayed in the right panel (b) of figure 13.

Next, we measured the intensity dependence of the beam loss with the operational parameters re-optimized for the 1.2-MW beam, as shown in figure 15, where the color variation shows a difference of the injection pulse length ($0.1 \sim 0.6$ ms), that is, a variation of the beam intensity ($0.2 \sim 1.2$-MW-eq). In this figure, one can find that most of the beam loss appears for the first 1 ms when the injection orbit bump is active for charge-exchange injection. In addition, we can confirm that the beam loss has a linear response for a product of the beam intensity and the foil hitting rate during charge-exchange injection. Namely, the experimental data show that most of the residual beam loss originates from foil scattering during charge-exchange injection, namely that the other major beam loss, arising from resonant phenomena, is satisfactorily minimized for the beam intensities of up to 1.2-MW-eq.

Following the above beam test, we conducted a similar 1.2-MW beam test with a higher injection peak current of 60 mA in Dec. 2018, where the injection pulse length was maintained at the original value of 0.5 ms. Owing to the increase in the peak current, the injection beam emittance increased by several 10%, but it did not lead to significant additional beam loss in the RCS; we got almost the same results as those in figures 13 and 15 also in this beam test.

Although the beam acceleration still remains at 1 GeV due to a hardware limit of the present rf system, these experimental results clearly demonstrate that the RCS has a sufficient potential to realize high-power beam operations of 1.2 MW or more from the beam dynamics viewpoint.

2020 JINST 15 P07022

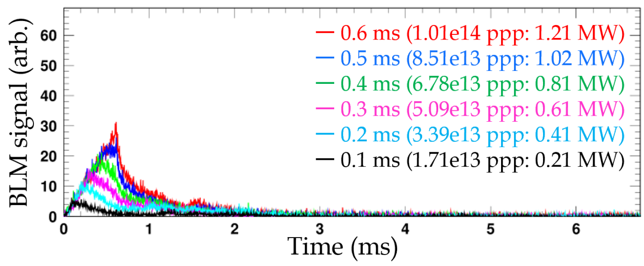

Figure 15. Beam loss monitor signals at the collimator section measured for the beam intensities from 0.2 MW to 1.2-MW-eq.

4 Numerical simulation studies to explore the intensity limit of the RCS

A 1.2-MW beam operation has come into view. Therefore, our interest now shifts to matters concerning the intensity limit of the RCS. In this section, we report our investigations into what finally limits the RCS beam intensity, based on numerical simulations of up to 3 MW.

Figures 16 (a) and (b) show the intensity dependences of beam loss and transverse rms emittances calculated with the operational parameters optimized for the 1.2-MW beam. As shown in the figures, beam loss sharply increases involving emittance blow-up after a 2-MW-eq beam intensity.

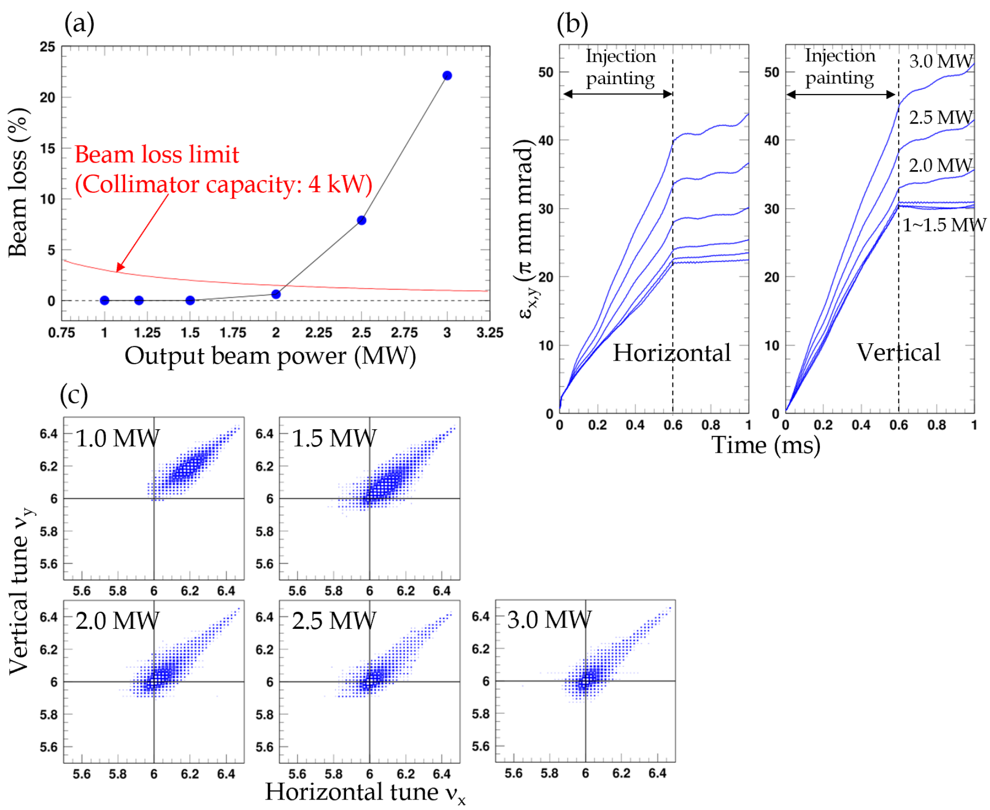

Figure 16. Numerical simulation results; (a) beam losses, (b) transverse rms emittances, and (c) tune footprints at the end of injection, calculated for the beam intensities from 1 MW to 3-MW-eq.

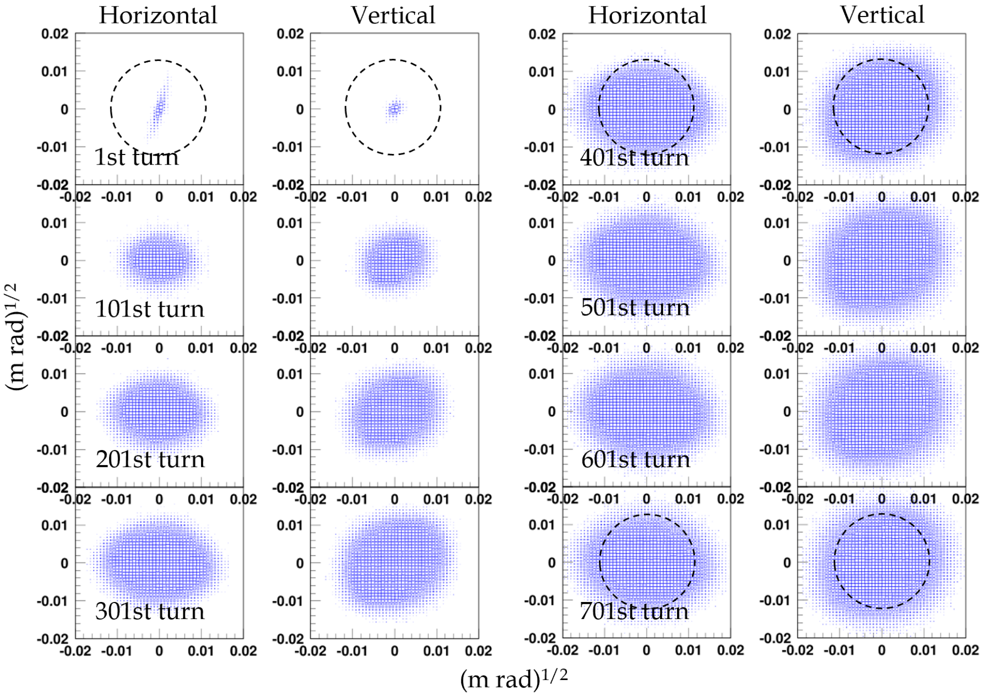

Figure 17. Numerical simulation results; transverse phase-space distributions from 1st turn to 701st turn calculated for the beam intensity of 3-MW-eq, where the dotted circles show the painting area, and the 401st turn is right after the end of injection painting.

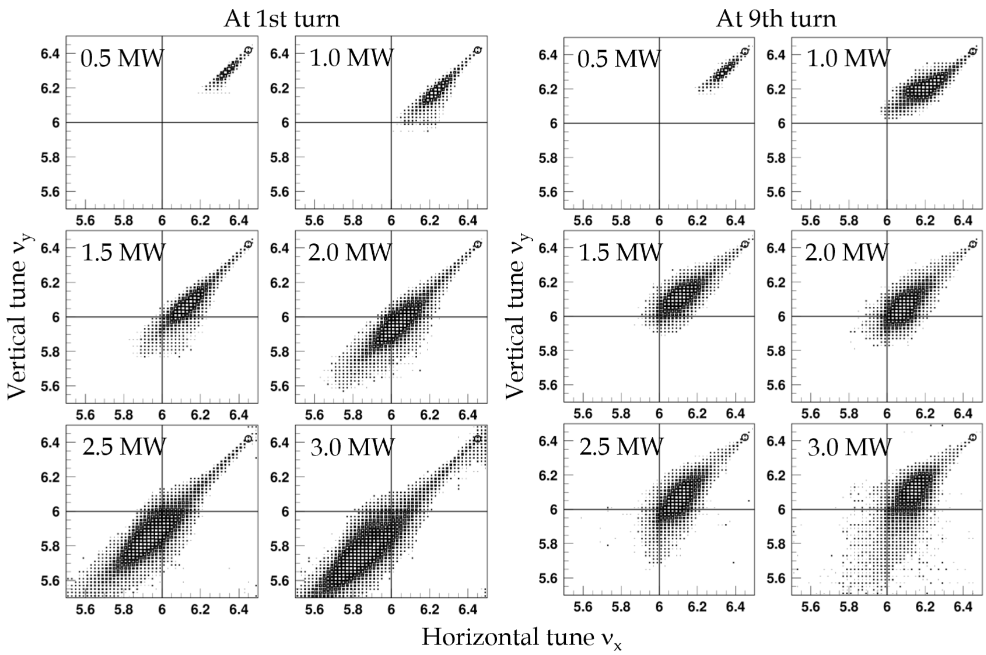

Figure 18. Results of the 1-turn injection simulations; tune footprints at the 1st turn (left) and 9th turn (right), calculated for the beam intensities from 0.5 MW to 3-MW-eq.

Figure 16 (c) shows the intensity dependence of tune shift calculated at the end of injection, in which one can find that the emittance blow-up observed after a 2-MW-eq beam intensity compensates the increase of tune shift; there are no significant differences among the tune shifts after a 2-MW-eq beam intensity. The integers $\nu_{x,y} = 6$ look like a barrier preventing the increase of tune shift.

In order to find the cause of the sharp rise of beam loss, we first investigated the turn-by-turn evolution of the transverse phase-space distribution, as shown in figure 17. In the figure, one can confirm that a large emittance growth occurs over the painting area, but cannot get any more useful information from this. Multi-turn injection painting may conceal the mechanism of the emittance blow-up. Hence, we next performed simpler simulations omitting the injection painting process, namely, 1-turn injection simulations. In the simulations, the initial 6d distribution was made beforehand, separately performing injection painting simulation with no space charge. Then, it was 1-turn injected with space charge, and its subsequent behavior was investigated.

Figure 18 displays the results of the 1-turn injection simulations, showing the intensity dependence of tune shift calculated at the 1$^{\text{st}}$ turn and 9th turn. As shown in the figure, the tune shift at the 1$^{\text{st}}$ turn occurs proportionally to the beam intensity. But, after 9 turns, the situation drastically changes, where the large tune shifts observed for the beam intensities of more than 2-MW-eq are pushed back above the integer. This situation is comparable with that in figure 16 (c). It shows that a large emittance blow-up occurs for the beam intensities of more than 2-MW-eq also in the 1-turn injection simulation, similarly to that in figure 16 (b).

Figure 19 shows the transverse phase-space distributions at the 5th turn, calculated for the beam intensities from 0.5 MW to 3-MW-eq. As shown in the figure, the beam distributions are almost stable up to 1.5 MW, but significant deformation of the beam distribution shows up after 2 MW. Although most of the beam losses that we have encountered in the 1-MW beam tuning can be

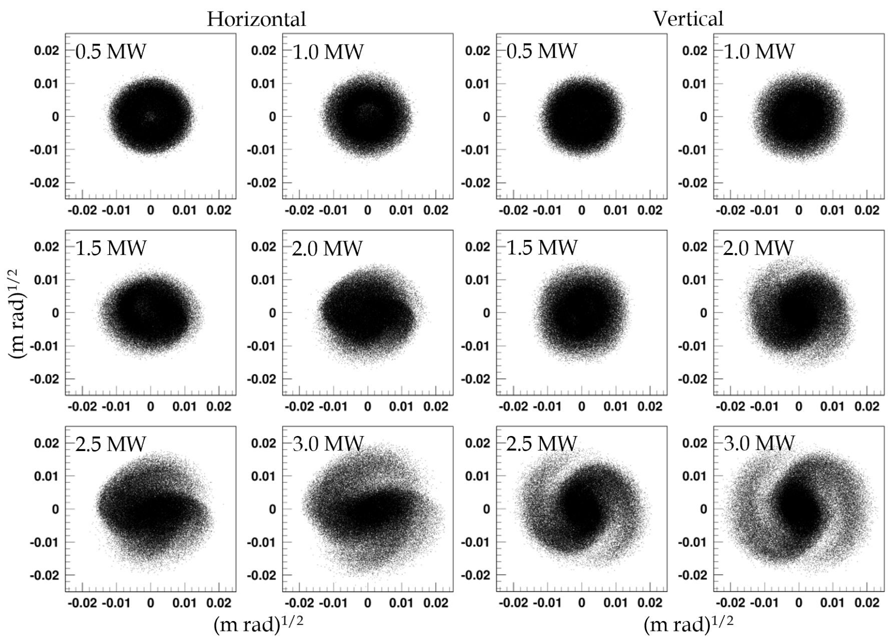

Figure 19. Results of the 1-turn injection simulations; transverse phase-space distributions at the 5th turn, calculated for the beam intensities from 0.5 MW to 3-MW-eq.

2020 JINST 15 P07022

ascribed to "incoherent" resonances as discussed above, the characteristic deformation of the whole beam distribution suggests that it is caused by the 2nd-order "coherent" resonance. The coherent resonant condition is expressed as $2(\nu_0 - C_2 \Delta\nu) = 12$ [18, 19], where ν_0 is the bare betatron tune, $\Delta\nu$ the rms tune shift, and C_2 the coherent tune shift factor, which has a value of < 1 depending on the operational condition, the initial beam distribution, etc. It appears that the observed deformation of the beam distribution occurs when the rms tune shift reaches below the integer following the coherent resonant condition.

The 1-turn injection simulations suggest that the large emittance growths observed after 2 MW in the realistic numerical simulations including the painting process (figure 16) can also be attributed to the 2nd-order coherent resonance, namely that the coherent resonance could be one of the key factors limiting the beam intensity achievable in the RCS. A hypothesis that such a low-order coherent resonance sets the intensity limit is quite reasonable, but we have not yet found clear evidence for this. As already mentioned in figure 17, the multi-turn injection painting process makes it difficult to observe the resonance phenomenon distinctly. Therefore, the next major subject in our beam studies is to find signs of the coherent resonance in the complex injection painting process, which will be the key to understanding the intensity limit of the RCS.

5 Summary

We launched a full-scale 1-MW beam test in Jan. 2015. Since then, we have developed beam studies for beam loss mitigation. Most of the beam losses that we have encountered in 1-MW beam tuning were ascribed to incoherent resonance phenomena. Numerical simulation played a vital role, not only in solving such beam loss mechanisms but also in finding their solutions in combination with actual beam experiments; various ideas for beam loss mitigation were proposed with the help of the numerical simulations and verified by experiments. As a result of these continuous efforts, including several hardware improvements, we have recently accomplished the 1-MW design beam operation with considerably low fractional beam loss of several 10^{-3}.

In addition, following the success of the 1-MW beam demonstration, we have recently initiated further high-intensity beam studies towards a higher beam power beyond 1 MW. The beam tests conducted in Oct. and Dec. 2018 showed promising results on the feasibility of a 1.2-MW beam operation. In parallel with the beam experiments, we also conducted beam simulations of up to 3 MW to explore the intensity limit of the RCS. The numerical simulations showed the sharp rise of beam loss after a 2-MW-eq beam intensity, and implied that it is caused by the 2nd-order coherent resonance; it means that the coherent resonance could be one of the important factors limiting the achievable beam intensity in the RCS. However, we have not yet obtained conclusive evidence for this; multi-turn injection painting applied for the RCS complicates isolating the issue. We will continue both experiments and numerical simulation studies to get a clear conclusion on the intensity limit of the RCS, and to lead the findings to a further performance upgrade of the RCS.

Acknowledgments

The authors acknowledge Dr. K. Hasegawa, Prof. T. Koseki, and all the RCS group members for their continuous support and encouragement for the present work. We are also grateful to the linac and 3NBT group members for their indispensable support during the beam experiments, and to Dr. S. Machida for his valuable advice and continuous support for the numerical simulation and the analysis. The authors also acknowledge Prof. Y. Yamazaki, Prof. A. Ando, Prof. Y. Irie, Prof. E. Takasaki, and Prof. K. Oide for their continuous support and sharp advice for the RCS beam commissioning and operation.

References

[1] High-intensity Proton Accelerator Project Team, *Accelerator Technical Design Report for High-intensity Proton Accelerator Facility Project*, J-PARC, JAERI-Tech-2003-044.

[2] H. Hotchi et al., *Beam commissioning of the 3-GeV rapid cycling synchrotron of the Japan Proton Accelerator Research Complex*, *Phys. Rev. ST Accel. Beams* **12** (2009) 040402.

[3] H. Hotchi et al., *Achievement of a low-loss 1-MW beam operation in the 3-GeV rapid cycling synchrotron of the Japan Proton Accelerator Research Complex*, *Phys. Rev. Accel. Beams* **20** (2017) 060402.

[4] S. Machida and M. Ikegami, *Simulation of space charge effects in a synchrotron*, *AIP Conf. Proc.* **448** (1998) 73.

[5] F. Tamura, M. Yamamoto, C. Ohmori, A. Schnase, M. Yoshii, M. Nomura et al., *Multiharmonic rf feedforward system for beam loading compensation in wide-band cavities of a rapid cycling synchrotron*, *Phys. Rev. ST Accel. Beams* **14** (2011) 051004.

[6] B.W. Montague, *Fourth-order coupling resonance excited by space-charge forces in a synchrotron*, CERN-68-38, CERN (1968).

[7] I. Hofmann, *Stability of anisotropic beams with space charge*, *Phys. Rev.* **E 57** (1998) 4713.

[8] H. Hotchi, *Effects of the Montague resonance on the formation of the beam distribution during multiturn injection painting in a high-intensity proton ring*, *Phys. Rev. Accel. Beams* **23** (2020) 050401.

[9] H. Hotchi et al., *Beam loss reduction by injection painting in the 3-GeV rapid cycling synchrotron of the Japan Proton Accelerator Research Complex*, *Phys. Rev. ST Accel. Beams* **15** (2012) 040402.

[10] H. Hotchi, H. Harada and T. Takayanagi, *J-PARC RCS: High-Order Field Components Inherent in the Injection Bump Magnets and Their Effects on the Circulating Beam During Multi-Turn Injection*, *J. Phys. Conf. Ser.* **1350** (2019) 012102.

[11] T. Takayanagi et al., *Measurement of the injection bump magnets at J-PARC 3 GeV RCS*, in *Proceedings of the 4th Annual Meeting of Particle Accelerator Society of Japan*, Wako, Japan, 1–3 August 2007, pp. 85–87.

[12] H. Harada et al., *Modeling for the injection bump system at the J-PARC 3 GeV Rapid Cycling Synchrotron*, in *Proceedings of the 4th Annual Meeting of Particle Accelerator Society of Japan*, Wako, Japan, 1–3 August 2007, pp. 88–90.

[13] H. Harada, *Painting-injection study using a virtual accelerator in a high-intensity proton accelerator*, Ph.D. Thesis, Hiroshima University (2009).

[14] F. Tamura et al., *Longitudinal painting with large amplitude second harmonic rf voltages in the rapid cycling synchrotron of the Japan Proton Accelerator Research Complex*, *Phys. Rev. ST Accel. Beams* **12** (2009) 041001.

[15] M. Yamamoto et al., *Simulation of longitudinal beam manipulation during multi-turn injection in J-PARC RCS*, *Nucl. Instrum. Meth.* **A 621** (2010) 15.

[16] M. Yamamoto, M. Furusawa, K. Hara, K. Hasegawa, M. Nomura, C. Ohmori et al., *Conceptual Design of a Single-Ended MA Cavity for J-PARC RCS Upgrade*, *J. Phys. Conf. Ser.* **1067** (2018) 052014.

[17] M. Yamamoto et al., *Vacuum tube operation analysis for 1.2 MW beam acceleration in J-PARC RCS*, in *Proceedings of IPAC19*, Melbourne, Australia, 19–24 May 2019, TUPTS035.

[18] H. Okamoto and K. Yokoya, *Parametric resonances in intense one-dimensional beams propagating through a periodic focusing channel*, *Nucl. Instrum. Meth.* **A 482** (2002) 51.

[19] K. Kojima, H. Okamoto and Y. Tokashiki, *Empirical condition of betatron resonances with space charge*, *Phys. Rev. Accel. Beams* **22** (2019) 074201.